Two-phase hydrodynamics in a miniature direct methanol fuel cell

Cullen R. Buie [1], Juan G. Santiago [*]

Department of Mechanical Engineering, Stanford University, 440 Escondido Mall, Building 530, Room 225, Stanford, CA 94305, USA

ABSTRACT

We present controlled experiments on a miniature direct methanol fuel cell (DMFC) to study the effects of methanol flow rate, current density, and void fraction on pressure drop across the DMFC anode. We also present an experimental technique to measure void fraction, liquid slug length, and velocity of the two-phase slug flow exiting the DMFC. For our channel geometry in which the diameter of the largest inscribed sphere (a) is 500 μm, pressure drop scales with the number of gas slugs in the channel, surface tension, and a. This scaling demonstrates the importance of capillary forces in determining the hydrodynamic characteristics of the DMFC anode. This work is aimed at aiding the design of fuel pumps and anode flow channels for miniature DMFC systems.

© 2009 Elsevier Ltd. All rights reserved.

1. Introduction

Direct methanol fuel cells (DMFCs) are currently being explored for numerous applications including portable electronics and auxiliary power units (APUs). A key concern for all fuel cell systems is the balance of plant which may consists of pumps, power conditioning circuitry, and other auxiliary devices. In order to avoid the complexity associated with active fuel delivery systems, many DMFCs for portable applications employ passive fuel and/or oxidant delivery [1–6]. While passive systems reduce overall power plant complexity, they are generally highly sensitive to environmental conditions [1,2]. As a result, considerable effort has been devoted to passive transport in DMFC anodes, but relatively few studies detail design considerations for active fuel delivery systems. At the anode of a DMFC methanol is oxidized in the presence of water, yielding protons, electrons and CO_2 as follows:

$$CH_3OH + H_2O \longrightarrow CO_2 + 6H^+ + 6e^- \qquad (1)$$

Product CO_2 establishes a two-phase flow within the DMFC anode with potentially higher pressure loading than a single phase flow. For proper design of active fuel delivery systems, prediction of two-phase hydraulic resistance is a critical design criterion.

Two-phase flows arise in a wide range of engineering applications including refrigeration, oil recovery, and groundwater flow [3,4]. Numerous two-phase flow models have been proposed [3,5] but full analyses of these is outside the scope of this study.

Two-phase flows arise in many low temperature fuel cell applications but most studies focus on transport within the diffusion media [6–9]. However, two-phase flow and pressure drop have been explored in proton exchange membrane fuel cell (PEMFC) cathode flow channels due to the challenges of water management [10–13]. With respect to two-phase flow in DMFCs, there have been several studies related to two-phase transport in the anode gas diffusion layer (GDL) [14–17].

We will briefly summarize some of the work regarding two-phase flow pressure drop in DMFC anodes. Argyropoulos et al. [18] developed a homogeneous model for two-phase flow in a 272 cm^2 cell (they don't specify channel dimensions). Their work incorporated minor losses associated with the manifold in their parallel channel architecture. Their modeling study suggested that pressure drop in the anode is a non-linear function of inlet methanol flow rate, but was relatively invariant with current density. Recently, Yang et al. [19] explored pressure drop across a DMFC anode in a single serpentine channel. They employed a 2 × 2 mm square, 420 mm long channel and showed that for their system, orientation and gravitational effects strongly influence pressure drop. In the work of both Argyropoulos et al. [18] and Yang et al. [19], it is important to note that capillary forces could be neglected.

We considered and attempted to apply several general (i.e., not fuel cell specific) two-phase flow models to study our present results. These included a homogeneous flow model [4], and a Lockhart–Martinelli type separated flow model [4,5,20]. The homogeneous model, the simpler of the two, displays a monotonic increase in pressure drop with current density (at constant inlet methanol flow rate). The Lockhart–Martinelli type model also shows a monotonic increase in pressure but the predicted rate of increase is lower than the homogeneous model. We note that

---

* Corresponding author.
  E-mail address: juan.santiago@stanford.edu (J.G. Santiago).
[1] Present address: Department of Mechanical Engineering, Massachusetts Institute of Technology, 77 Massachusetts Avenue, Cambridge, MA 02139, USA.

Nomenclature

a	diameter of the largest inscribed sphere	R	universal gas constant
A_{FC}	fuel cell area	R_{xy}	cross correlation
Ca	capillary number	Re	Reynolds number
d_b	bubble detachment diameter	T	absolute temperature
D_h	hydraulic diameter	u	velocity
d_p	gas diffusion layer pore diameter	V	voltage
F	Faraday's constant	We	Weber number
g	gravitational acceleration	z	streamwise channel location
j	fuel cell current density		
L	length	*Greek*	
n	electrons per mole	α	void fraction
N_{slug}	number of gas slugs	θ	contact angle
Δp	pressure drop	μ	dynamic viscosity
p	local pressure	ρ	density
Q	flow rate	σ	surface tension

---

neither of these two-phase models was able to capture even the major trends of pressure drop versus flow rate and quality which we observe here and will discuss later as part of Figs. 5a and 9b.

In this study we are interested in pressure loads required for miniature liquid-fed DMFCs employing microchannels (defined below). We will show that pressure drop in two-phase microchannels exhibit behavior unlike DMFC anodes explored previously. In particular, we find that capillary forces and the number of gas slugs in the channel play significant roles in the pressure load across the anode. To elucidate the effects of CO_2 generation we perform a detailed parametric study of the hydrodynamic coupling between fuel flow and fuel cell operation while measuring pressure drop, the number of gas slugs exiting the anode, and slug velocity at the channel outlet.

2. Scaling considerations

Surprisingly, there is a dearth of analysis of two-phase pressure drop in DMFC anode flow channels, particularly for microchannels. We here apply the prefix "micro" to two-phase flow channels if the diameter of the largest inscribed sphere is roughly the same as the bubble detachment diameter in freestream. For such channels, bubble detachment is strongly influenced by the channel geometry in addition to surface tension effects. The bubble detachment diameter (d_b) from a porous (GDL) surface can be estimated as [21,22],

$$d_b = \left(\frac{4 d_p \sigma \sin\theta}{g \left(\rho_l - \rho_g \right)} \right)^{1/3}. \tag{2}$$

Here, d_p is the GDL pore diameter, σ is surface tension, θ is contact angle, g is the gravitational acceleration, ρ_l is liquid density, and ρ_g is gas density. Assuming CO_2 emerges from a hydrophilic GDL ($\theta = 40°$) with 20 μm pores into a 2 mol/L methanol solution, d_b is approximately 680 μm. If CO_2 emerges from a hydrophobic GDL ($\theta = 110°$), with the same conditions as above, d_b is approximately 770 μm. In this study the diameter of the largest sphere inscribed in the anode flow channel is 500 μm, indicating that the channel walls will have a strong influence on gas slug/bubble detachment. Strong channel–wall interaction therefore distinguishes this study from previous studies on CO_2 evolution and pressure losses in DMFC anodes [18,19,21,23,24].

In Eq. (3) we follow the approach of Wong et al. [25,26] and write the conservation of momentum equation for the liquid phase traveling in an inertial frame of reference moving at the speed of the gas slugs,

$$We \rho^* u^* \frac{\partial u^*}{\partial x^*} = -\frac{\partial p^*}{\partial x^*} + Ca \frac{L}{a} \mu^* \left(\frac{\partial^2 u^*}{\partial y^{*2}} + \frac{\partial^2 u^*}{\partial z^{*2}} \right). \tag{3}$$

Here, density, ρ, velocity, u, streamwise position, x, pressure, p, dynamic viscosity, μ, and in-plane coordinates, y and z, are non-dimensionalized by local average density, ρ_o, local average velocity, u_o, channel length, L, surface tension divided by the diameter of largest inscribed sphere, σ/a, local average viscosity, μ_o, and the radius of largest inscribed sphere, a, respectively. In Eq. (3), an asterisk ($*$) denotes a non-dimensional parameter. Additionally, We is the Weber number $\rho_o u_o^2 a / \sigma_o$, and gives the relative scaling of inertial versus surface tension forces. We is the product of the Reynolds number (Re) and capillary number (Ca) where $Re = \rho_o u_o a / \mu_o$ (the ratio of inertial forces to viscous forces) and $Ca = \mu_o u_o / \sigma_0$ (the ratio of viscous forces to surface tension forces). Note that pressure is scaled as σ/a, which is the appropriate scaling for capillary pressure of a single channel-wide gas slug [27]. Although we will not solve it here, we present this equation as it suggests useful scaling arguments. In our system Ca (ratio of viscous to capillary forces) is very low ($Ca < 1 \times 10^{-4}$) so capillary forces are large compared with viscous forces. As shown in Eq. (3), pressure drop consists of both inertial and viscous losses. At the channel inlet, We is small compared to $Ca(L/a)$ (product of Ca and L/a) and viscous losses dominate. In this region, the flow resembles previous low Ca studies in which inertial effects are neglected [25–27]. Previous work has shown that at low Ca, with negligible inertial losses, pressure drop across a gas slug scales as ($Ca^{2/3}$) [25–27]. However, due to the introduction of CO_2 gas into the channel (resulting from the methanol oxidation reaction), the bulk fluid velocity increases downstream and inertial effects become more significant (i.e., since the stream accelerates as volume flow rate increases due to phase change). To first order, inertial effects become significant as $We \sim Ca(L/a)$, or $Re(a/L) \sim 1$ [where $Re(a/L)$ is the product of Re and (a/L)]. Again, this makes our system different than previous studies as here inertial forces are important. We will show that measured pressure data for our DMFC scales as σ/a; consistent with scaling for surface tension forces. Fig. 1 is a schematic of the assumed flow structure within the DMFC anode in a slug flow regime. The flow regime can be divided into two distinct regions; the first region contains a gas (CO_2) slug surrounded by a thin liquid annulus. The second region is a single phase liquid flow bound in the front and rear by CO_2 slugs.
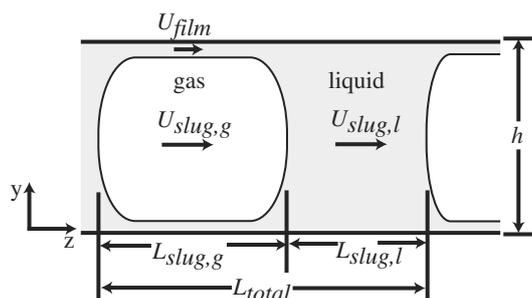
Fig. 1. Schematic of intermittent flow regime within the fuel cell flow channel. Numerous visualization studies [25,27,28] confirm that, at most current densities of interest, DMFC anodes exhibit a slug/intermittent flow pattern. For this study we assume that the ratio of $L_{slug,g}$ to L_{total} is roughly the void fraction in the channel (i.e., thin annular region).
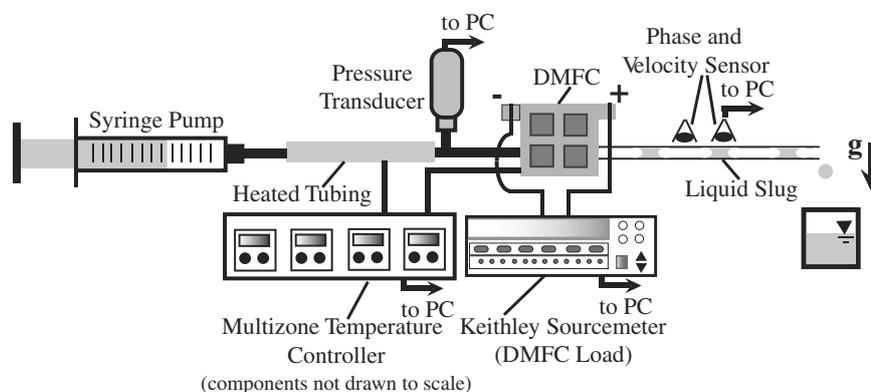
3. Experimental

To study and determine the relevant force scaling for the intermittent two-phase flow exiting the DMFC we designed an ex situ flow characterization system. Fig. 2 is a schematic of our DMFC experimental setup configured to measure liquid phase velocity and void fraction of the two-phase mixture exiting the fuel cell. The setup includes an electronic load (Keithley 2410 Sourcemeter), a custom temperature control unit, a syringe pump (Harvard Apparatus PHD 2200), a low range (0–10 in H_2O) differential pressure sensor (Omega PX-154), a function generator (Agilent 33120A), a data acquisition card (National Instruments PCI-3061E) with breakout box, and two liquid level sensors (Optek OPB350). The function generator serves as an external timing reference to trigger data acquisition from the phase/velocity (liquid level) sensors and pressure transducer. The electronic load operates in four-wire sense mode with the source and sense wires connected to the DMFC anode and cathode. The Keithley Sourcemeter is controlled via GPIB and integrated with LabView 8 using a National Instruments PCI-GPIB card.

Measurements of key parameters in two-phase flow, including mixture (or phase) velocity, void fraction (or quality), and pressure drop, are critical to the development of engineering models for pressure drop relationships and for validation of existing models. For this study we developed a method of measuring liquid phase velocity and volume fraction using the Optek optical liquid sensors mentioned above. These sensors are sold for process engineering applications and they essentially detect the presence of liquid (versus gas) in a tube using an infrared (IR) photodiode source and a photodiode detector. A high electric signal indicates high transmission of IR (liquid in a ~5 mm long channel section), while a low signal indicates low transmission (gas). The response of each sensor was evaluated with pure liquid and pure gas in order to determine the appropriate threshold voltage. We place two of these sensors a known distance apart (9.2 mm center-to-center) and determine liquid slug velocity, void fraction, and liquid slug length by signal processing (including time-delayed cross-covariance analysis). The sensors connect to the outlet of the DMFC through a 1.5 mm inner diameter Teflon tube. The tubing has a high contact angle (roughly 110°) and promotes separation of liquid and gas phases.

The optical void fraction technique is best illustrated by example in Fig. 3a and b. Here we show two sample time traces for sensors 1 and 2 in series (Fig. 3a). Shown are raw data of the intermittently high and low signals resulting from the passing of gas and liquid phases through the 1.5 mm ID exit tube of the DMFC. High voltage values (roughly 4.8 V) in both sensors correspond to liquid in the tube while lower values persist when gas is present. To determine void fraction we apply a simple threshold (halfway between the liquid and gas phase saturation voltages) to the time trace and designate values above the threshold as liquid phase. A sample raw cross correlation signal (not corrected for bias) used to determine time delay is shown in Fig. 3b. We determine slug velocities, u_{slug}, by the time delay of the highest peak of the cross-correlation, t_p ($u_{slug} = \Delta x / t_p$ where Δx is the distance between sensors). Average liquid slug lengths in the measurement tube are determined by analyzing individual low-to-high and high-to-low signal cross-over events. We use this information to estimate the length, number, and velocity of slugs near the exit of the anode channel (taking into account the area changes between the anode channel and the measurement tube). These data yield an estimate of the average number of gas slugs, N_{slug}, per fuel cell channel volume.

The DMFC used in this study is identical to the structure presented in a previous publication [28]. We use a commercially available 2 cm^2 membrane electrode assembly (BCS Fuel Cells, Bryan TX) with a 180 μm thick Nafion 117 electrolyte membrane and 350 μm thick diffusion media (carbon cloth). The anode and cathode catalyst loadings are 4 mg/cm^2 Pt–Ru and 2 mg/cm^2 Pt, respectively. The fuel cell utilizes a free convection cathode and the anode consists of a single serpentine flow channel. The channel is machined in house from a graphite plate and is 750 μm wide and 500 μm deep. The length of the channel is 13 cm. For this study

Fig. 2. Schematic of the experimental setup including free convection (cathode) DMFC, syringe pump, pressure transducer, phase/velocity sensors, multizone temperature controller, and Keithley Sourcemeter (providing fixed current density loads). With the exception of the syringe pump, the entire system is controlled via PC running LabView 8. The Keithley Sourcemeter communicates over GPIB while the phase/velocity sensors and pressure transducer interface through a data acquisition card (National Instruments PCI-3061E). A function generator (not shown) provides external triggering to facilitate precise synchronization of measurements from the phase/velocity sensors and pressure transducer.
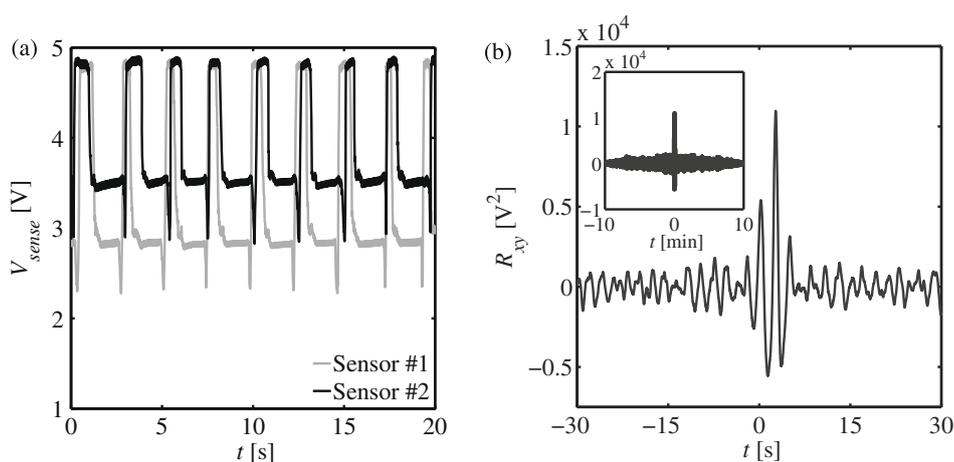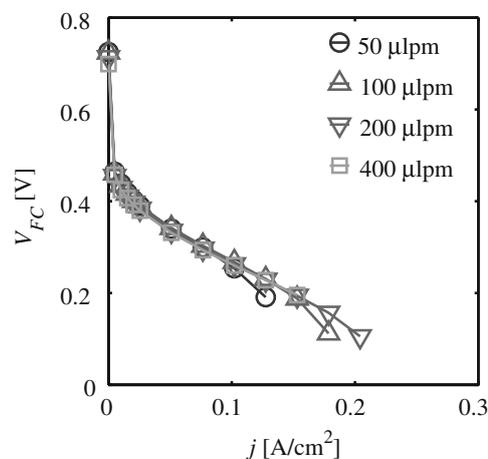
Fig. 3. Sample raw data (a) and cross correlation (b) for 1 mol/L methanol delivered at 100 μlpm to the DMFC operated at 0.15 A/cm^2. Shown here is raw data of the intermittently high and low signals resulting from the passing of liquid and gas phases through the 1.5 mm ID exit tube of the DMFC. High voltage values (roughly 4.8 V) in both sensors correspond to liquid in the tube while lower values indicate a gas filled tube. Panel (b) shows a sample raw cross correlation signal. Slug velocities are determined from the time delay peak of the cross-correlation (here 2.7 s).

we employed a single serpentine channel in order to isolate the effects of two-phase pressure drop without introducing the instabilities inherent with parallel and parallel/serpentine designs. In this study we employed constant inlet flow rate at the anode rather than constant anode stoichiometry. This is common practice in DMFC studies [17,19,21,24,29–32]. More importantly, constant flow rate with variable current allows us to sample a wide range of void fractions (from 0% to >90%), and thereby explore the effect of this critical parameter on pressure drop. As we will show in subsequent sections, we find that void fraction is perhaps the single most important parameter in determining overall pressure drop (most often more important than flow rate). A summary of the experimental conditions is given in Table 1. The materials and experimental conditions indicated in Table 1 apply to all experiments, unless otherwise specified. We characterize the pressure drop in the system while simultaneously performing polarization measurements across a wide range of operating conditions. For each polarization measurement we keep current density constant as CO$_2$ production (and subsequently pressure drop, velocity, and void fraction) is mostly a function of current density.

4. Results and discussion

As indicated in Table 1, we performed 16 total polarization curves for four methanol concentrations and four inlet flow rates. In most of the data presented here, we emphasize a representative subset of the cases studied: 1 mol/L methanol concentration supplied at 50, 100, 200, and 400 μlpm. We found that methanol concentration had a strong effect on the electrochemical performance of the DMFC (e.g., due to methanol crossover) [14,32–35] but had a
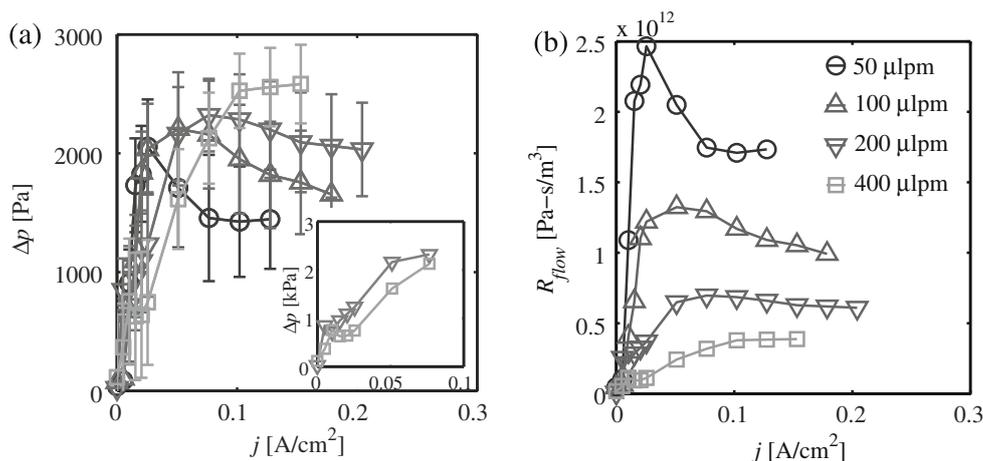
relatively small effect on the hydrodynamics in the anode. In Fig. 4 we present polarization curves at 1 mol/L methanol concentration. In the low current density regime (<0.1 A/cm^2) the cell potential (V_{FC}) is virtually invariant with methanol flow rate. This suggests DMFC performance is relatively insensitive to mass transfer effects in this regime. In contrast, mass transfer losses in the anode reduce cell potential at higher current densities (>0.1 A/cm^2). We attribute the reduced potentials to anode mass transfer losses for two reasons. First, in independent experiments with our air breathing fuel cell, we supplied hydrogen gas to the anode and observed a limiting current density on the order of 0.5 A/cm^2 (so there is likely sufficient oxygen available at the current densities represented in Fig. 4). Second, the DMFC limiting current density generally increases with increasing inlet flow rate, as expected. Mass transfer limitation in Fig. 4 is further confirmed by experiments we performed at 0.5 mol/L concentration and 50, 100, and 200 μlpm flow rates (not shown here). The associated measured maximum current density with 0.5 mol/L methanol was, at each flow rate, lower than the corresponding maximum current density with 1 mol/L

Table 1
Experimental parameters.

Parameter	Value
Fuel cell electrolyte	Nafion 117
Gas diffusion layer	350 μm E-Tek anode and cathode
Active area	2 cm^2
Anode channel dimensions	750 μm × 500 μm × 13.1 cm ($W \times H \times L$)
Catalyst loading	4 mg/cm^2 Pt–Ru anode, 2 mg/cm^2 Pt cathode
Methanol concentration	0.5, 1, 2, 4 mol/L
Anode flow rate	50, 100, 200, 400 μlpm
Cathode gas	Atmospheric air
Fuel cell temperature	50 °C

Fig. 4. Polarization curves for 1 mol/L aqueous methanol supplied at 50 (○), 100 (△), 200 (▽) and 400 (⊡) μlpm. With the exception of the 400 μlpm case, the limiting current density of the DMFC increases with increasing inlet fuel flow rate. At low current densities (<0.1 A/cm^2) cell polarization is virtually identical across the four flow rates, indicating negligible mass transfer effects (e.g., due to fuel starvation or methanol crossover).

Fig. 5. Measured anode pressure drop (a) and flow resistance (b) as a function of DMFC current density, j. The legend in (b) also applies to (a). For each flow rate, as current density increases pressure drop (and flow resistance) reaches a maximum. Subsequent increase in j reduces the pressure load and flow resistance. The error bars shown in (a) represent two standard deviations of the time-averaged pressure measurement. The error bars are included to highlight the temporal fluctuations in pressure across the anode. In the inset of (a) we show that there is a small horizontal region (at $j < 0.05$ A/cm^2) in the measured pressure for the 200 and 400 μlpm cases. We attribute this region to a transition from bubbly to slug flow regimes in the anode channel.

methanol. In fact, the 1 mol/L maximum currents at 50, 100, and 200 μlpm are 100%, 100%, and 78% higher, respectively, than the corresponding 0.5 mol/L cases. This supports our hypothesis that the operation of our cell as shown in Fig. 4 is limited by mass transport. We note that the 400 μlpm case unexpectedly showed a lower current density range than the 100 and 200 μlpm polarization curves. This trend (lower current densities for the 400 μlpm case) was repeated in future experiments at other methanol concentrations. In future work we plan to explore whether this phenomena is an artifact of our experimental setup and control or if it points to relevant physics of our DMFC's operation.

Fig. 5a and b shows measured pressure drop and corresponding flow resistance across the DMFC anode. Beginning with the total pressure drop across the anode (Fig. 5a) we highlight several interesting trends. Note that pressure drop at 0 A/cm^2 is very small compared to pressure drop at high current density, although finite. First, at low current densities the lowest inlet methanol flow rate has the highest pressure drop. This counterintuitive behavior is also apparent in Fig. 5b where the flow resistance of the 50 μlpm case is an order of magnitude higher than the flow resistance at 400 μlpm. Next, with increasing current density, each case reaches a maximum pressure load and then begins to decrease. At higher current densities (>0.1 A/cm^2), the highest flow rate has the highest pressure drop. Factors influencing and leading to these trends are discussed together with Fig. 6.

In Fig. 6 we present measurements of anode exit bulk velocity (Fig. 6a), liquid slug length (Fig. 6b), void fraction (α) at the anode exit (Fig. 6c), and the average number of gas slugs per volume of fluid equal to the channel volume (N_{slug}) (Fig. 6d). (Each unit cell depicted in Fig. 1 is counted as one slug.) Note that our technique cannot measure velocity of a single phase flow; and so we have no data for and do not plot a velocity measurement at 0 A/cm^2 in Fig. 6a. The anode exit velocities are approximately directionally proportional over the range of current densities explored (although only roughly true for the 400 μlpm case). A proportional dependence in velocity is expected since CO$_2$ mass (and volume) flow rate is a linear function of current density. Fig. 6b shows measured liquid slug length as a function of current density (note slug length is shown on a logarithmic scale). For each fixed current density, longer slug length corresponds to the higher inlet flow rate. This is expected as higher inlet methanol flow rate results in lower void fraction and larger liquid slugs. In addition, for a given methanol

flow rate, liquid slug length decreases with increasing current density. Higher current density corresponds to higher gas flow rate and higher aqueous methanol consumption, both of which yield smaller/shorter liquid slugs.

Fig. 6c shows largely expected trends in exit void fraction; mainly that higher void fractions correlate with higher current density and lower methanol flow rate. Finally, with respect to DMFC performance and pressure load, Fig. 6d presents the most interesting phenomena. Here we plot the average number of gas slugs exiting the anode channel as determined from our phase and velocity measurement technique. The key observation here is that current density at maximum pressure load is correlated with the current density that possesses the largest average number of gas slugs. For example, compare Figs. 5a and 6d. This evidence suggests that the dominant physical feature contributing to pressure drop through the anode is the total number of gas slugs within the flow channel.

As shown by the data of Fig. 6c, void fraction curves all have similar dependence on current density, but significantly different magnitude. This trend was consistent across all four methanol concentrations explored (including 0.5, 2, and 4 mol/L in addition to the 1 mol/L data shown in Fig. 6). Void fraction should be a direct function of phase volume flow rate ratio; and this should be consistent with electric current and inlet flow rate measurements. Fig. 7 shows measured void fraction at the exit, for all four methanol concentration studies (and all flow rates), versus the ratio of calculated volume flow rate of CO$_2$ to measured inlet methanol volume flow rate. The estimate rate of gaseous CO$_2$ generation is a simple function of DMFC current density, $Q_{CO_2} = \frac{jA_{FC}RT}{nFp}$, where A_{FC} is fuel cell area, R is the universal gas constant, T is absolute temperature, and p is pressure (we assume atmospheric pressure). We see that the data for all 16 conditions (four inlet methanol flow rates and four concentrations) collapses nicely to a single curve. This shows that the experimental setup obtained repeatable measurements with respect to void fraction for all conditions. We will later leverage an empirical fit to the curve in Fig. 7 to predict pressure drop across all conditions.

As described above, we directly measure the number of slugs exiting the DMFC anode. We hypothesize that the outlet density of slugs (slug number per unit channel volume) is approximately the same in the outlet and throughout most of the anode channel length. This hypothesis is in agreement with and supported by the
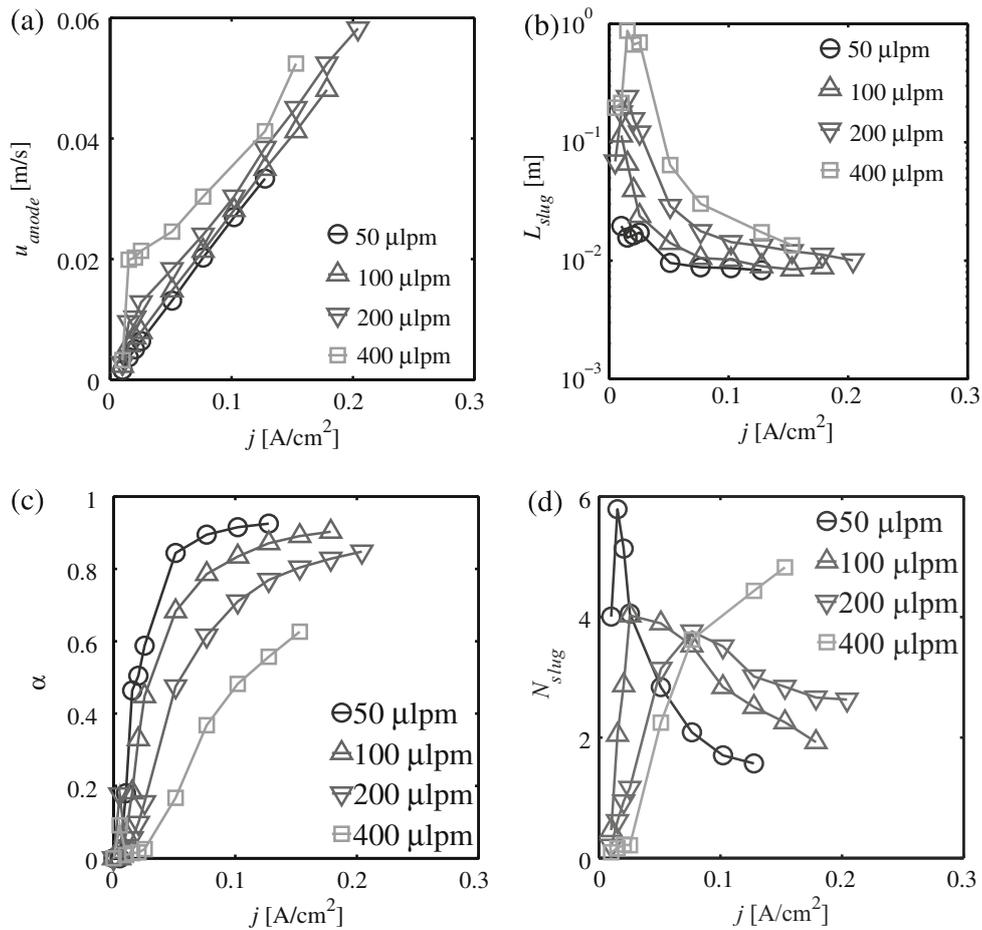
Fig. 6. Measured anode exit velocity (a), average liquid slug length (b), void fraction (c), and average number of gas slugs in the anode (d). As expected, measured exit velocity at the anode is a linear function of current density (a). Liquid slug length decreases as a function of current density (b) while void fraction increases (c). Interestingly, the trends in the number of slugs measured (d) follow the trends in total pressure drop (Fig. 5a).

results of, for example, Yang et al. [19,24] who visualized the entire DMFC anode.[2]

As we discussed earlier, low void fractions are associated with low values of $Re(a/L)$ due to the relatively low flow rate of liquid methanol. High void fractions imply stronger inertial effects and finite values of $Re(a/L)$ (due to increased CO_2 flow rate). As shown in Fig. 8, this results in a monotonic increase in measured $Re(a/L)$ as a function of measured void fraction for the 16 cases explored in this study. $Re(a/L)$ is calculated from the measured exit velocity at the anode (see the example shown in Fig. 6a for 1 mol/L methanol concentration). To our knowledge, no previous studies explore this transition either theoretically or experimentally [25–27, 36]. There is a strong need for extensions of low Ca, two-phase flow theory to flows with finite (near unity) $Re(a/L)$ which span both viscous and inertial regimes.

In an effort to summarize the trends in pressure drop in the DMFC anode and explore the use of an *ad hoc* (to our flow architecture) pressure drop model, we've explored several scalings of the experimental data. This included quantification of the effects of the number of gas slugs, N_{slug}, per channel volume and the scaling of pressure drop across the anode. We present results of this scaling analysis in Fig. 9.

Fig. 9a shows the average number of slugs per channel volume of fluid (at a given time) versus void fraction (N_{slug} versus α for all cases (cf. Table 1). Representative uncertainty bars are shown in the inset for the 1 mol/L, 200 μlpm flow rate case. The uncertainty
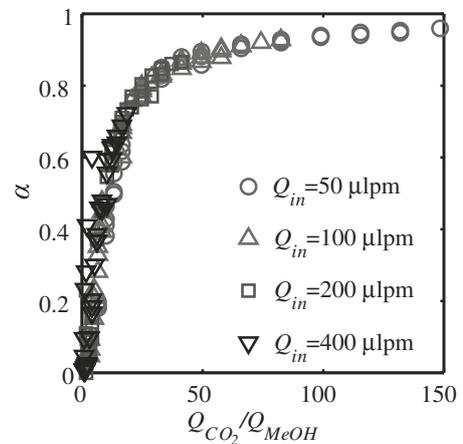
Fig. 7. Measured void fraction (α) versus ratio of CO_2 production rate (a function of current density) to inlet methanol solution flow rate. The plot includes data from 16 different cases, four flow rates (50, 100, 200, and 400 μlpm) and four methanol concentrations (0.5, 1, 2, and 4 mol/L). As shown, void fraction measurements show very good agreement across all explored cases.

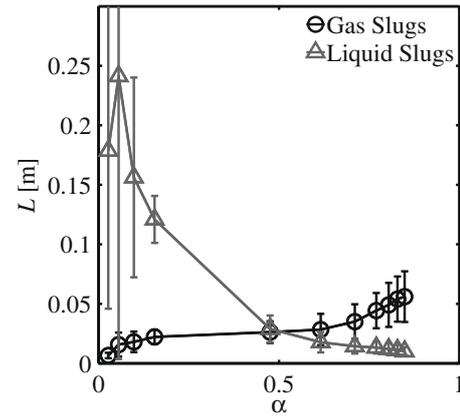[2] In reaching this conclusion, we analyzed the images of Yang et al. [19,24], and plotted their observed number of slugs versus current density. The images from both of their papers show trends very similar to the 100 and 200 μlpm data shown in Fig. 6d. We use this hypothesis (number of exiting slugs is approximately equal to that of internal slugs) to guide some of the scaling analyses we discuss below.
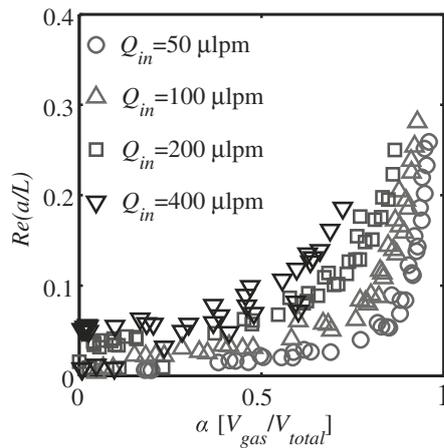
Fig. 8. $Re(a/L)$ (product of Re and a/L) versus measured void fraction for all 16 cases explored (cf. Table 1). As shown, $Re(a/L)$ increases monotonically with void fraction. As void fraction increases, $Re(a/L)$ approaches unity, suggesting that inertial effects become increasingly relevant [as shown in Eq. (3)].

Fig. 10. Measured gas ($\bigcirc$) and liquid ($\triangle$) slug lengths as a function of void fraction, α, for the 1 mol/L, 200 µlpm case. Uncertainty bars represent 95% confidence intervals and exhibit increased uncertainty due to a lower number of measurements at low α (e.g., 16 slug pairs at $\alpha = 0.098$, compared to 420 at $\alpha = 0.8$). As expected from the trends of Fig. 9, liquid slug length decreases while gas slug length increases with increasing void fraction. Further, gas and liquid slug lengths are roughly equal at $\alpha = 0.5$.

bars present the 95% confidence interval assuming a t-distribution. The low α range has the highest uncertainty due to the low number of slugs detected (e.g., 16 slugs at $\alpha = 0.098$ versus 420 slugs at $\alpha = 0.80$). At low α (i.e., low current density and associated CO_2 production), we see that N_{slug} increases with increasing gas volume in the channel; showing that initially, increases in CO_2 gas generation results in an increased number of gas slugs. N_{slug} reaches a maximum at about $\alpha = 0.55$, where gas and liquid slug volumes are roughly equal. The decrease in N_{slug} after $\alpha = 0.55$ suggests that new gas is being incorporated into previously formed/existing gas slugs in the anode channel. At near unity values of α, N_{slug} trends sharply downward to a minimum value of about 0.9 at the highest α measured, 0.96. This limiting behavior suggests that, at high α, the CO_2 generated along much of the anode channel length is recruited into large, already-existing gas slugs.

Before discussing Fig. 9b, we note that the trends of liquid and gas slug lengths suggested by Fig. 9a are confirmed by Fig. 10. For increasing α, Fig. 10 shows gas and liquid slug lengths have nearly monotonic increase and decrease, respectively. At low void fraction, liquid slug length decreases rapidly as gas bubbles are introduced into the otherwise liquid stream. The liquid and gas slug lengths are approximately equal at $\alpha = 0.5$, as expected. Beyond

$\alpha = 0.5$, liquid slug length continues to decrease, even though the number of gas slugs decreases (cf. Fig. 9a); again suggesting gas is recruited into already existing gas slugs. The slight apparent decrease in liquid slug length at high α is perhaps due to liquid consumption at the anode [both methanol and water as per Eq. (1)].

Next, we present scaled pressure drop in the anode in Fig. 9b. We found the best collapse of the data and most clear demonstration of trends by concentrating on the estimated pressure associated with each liquid/slug interface, $\Delta p_{total}/N_{slug}$, where Δp_{total} is the total pressure across the anode. This suggests that pressure drop in this system is dominated by capillary forces on individual gas slugs in the anode. We therefore also scale Δp_{total} using the capillary pressure scale σ/a (where a is the diameter of the largest sphere inscribed in the channel). Scaling total pressure with capillary pressure showed the best collapse of all of the data (particularly in the important mid-to-high range void fraction regime). The scale $\Delta p_{total}a/N_{slug}\sigma$ shows that the pressure drop per gas slug initially decreases at low void fraction. We see significant scatter at low α which we attribute to uncertainty in our N_{slug} measurements (cf. Fig. 9a). $\Delta p_{total}a/N_{slug}\sigma$ increases at higher α, after reaching a minimum at roughly $\alpha = 0.6$. Note $\Delta p_{total}a/N_{slug}\sigma$ reaches a
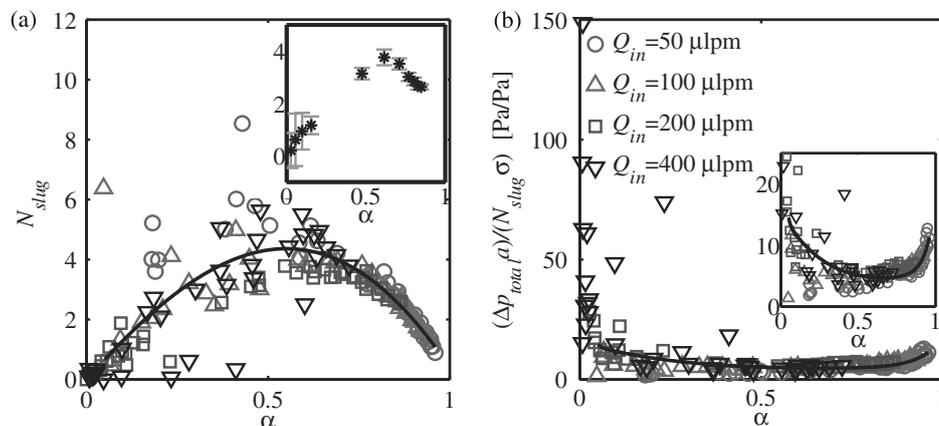
Fig. 9. Number of gas slugs (N_{slug}) (a) and scaled pressure drop per gas slug, $\Delta p_{total}a/N_{slug}\sigma$, (b); both as a function of measured void fraction, α, at the DMFC outlet. The legend in (b) applies (a) as well. In (a) we show the 1 mol/L, 200 µlpm case with error bars (95% confidence interval from t-distribution) in the inset. As α increases the error bars in (a) become smaller due to the higher number of slugs that pass the sensor (resulting in improved statistical certainty at high α). In (b), the pressure scaling is particularly effective for α greater than 0.6. The uncertainty in N_{slug} at low void fraction values causes greater scatter in the low void regions of $\Delta p_{total}a/N_{slug}\sigma$.
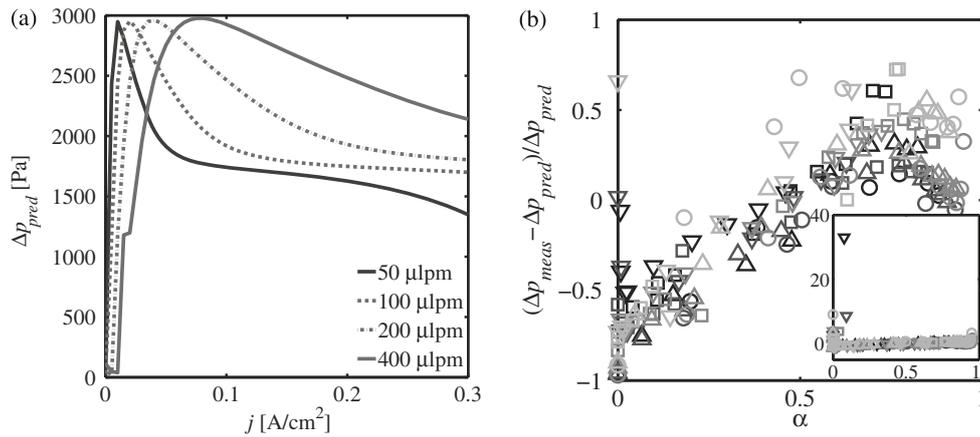
Fig. 11. Predicted pressure drop for the 50, 100, 200, and 400 μlpm cases (a) and the normalized difference between the model prediction and measured pressure (b). In (b) different shades represent the four concentrations studied and the symbols represent the 50 (○), 100 (△), 200 (▽) and 400 (□) μlpm cases. The predicted pressure follows the general trends shown experimentally for pressure (Fig. 5a). Note that the small 'notch' in pressure for the 400 μlpm case is also seen in the experimental data (cf. inset of Fig. 5a). In the inset of (b) we show that at very low α (<0.1), the difference between predicted, Δp_{pred}, and measured pressure, Δp_{meas}, is significantly larger than at higher α (>0.5). The improved correlation at high α is partly due to improved statistical certainty of the measurements (cf. Figs. 9 and 10). Further, as shown in the main axes of (b), the model generally over predicts pressure drop at α < 0.5 and under predicts pressure drop at α > 0.5.

minimum at roughly the same void fraction where N_{slug} reaches a maximum. This suggests that $\Delta p_{total} a / \sigma$ is roughly constant, at least in the moderate α range (again implicating the importance of capillary pressure effects).

We note the effectiveness of capillary scaling discussed above is consistent with the work of Bretherton [27], Wong et al. [25,26], and Fuerstman et al. [36] who found that pressure drop scales with the capillary force on the bubble/slug interface in low capillary number ($Ca < 5 \times 10^{-3}$) flows. We further note that we have previously explored [37] the applicability of a two-phase homogeneous flow [4] and a Lockhart–Martinelli type separated flow model [20] to explain the trends in our data. However, we found these models under-predict anode pressure drop by nearly an order of magnitude. Also, these models predict a strictly monotonic trend of pressure drop with increasing void fraction, while our experiments clearly show a pronounced maximum value. Evidently, these two-phase flow models (which neglect capillary pressure) fail to capture the underlying physics of flow in our DMFC anode.

We explored a few curve fits for N_{slug} (Fig. 9a) and the scaled pressure drop data (Fig. 9b). We found adequate agreement for N_{slug} with a fourth-order polynomial fit of the form,

$$N_{slug} = 2.3\alpha^4 - 10\alpha^3 - 5.4\alpha^2 + 14\alpha. \tag{4}$$

The pressure data was sufficiently well characterized by a dual exponential fit of the form,

$$\Delta p_{total} \frac{a}{N_{slug}\sigma} = (1-\alpha)[15 \cdot \exp(-2.2\alpha) + 130 \cdot \exp(-93\alpha)]$$
$$+ (\alpha) \cdot \left[4.9 \cdot \exp(0.11\alpha) + 4.0 \cdot 10^{-7} \cdot \exp(17\alpha)\right]. \tag{5}$$

These fits are shown in Fig. 9a and b as solid lines. We present these only as *ad hoc* empirical determinations of pressure drop and the number of slugs for the purpose of engineering estimates and optimization of DMFC performance. Further work is needed before we can conclude that these shapes are fairly general to these flow regimes.

Using the empirical correlations for N_{slug} [Eq. (4)] and pressure drop due to each gas slug [Eq. (5)], we can fairly predict the pressure drop in the anode as a function of current density. Here we assume that the pressure drop in the anode is dominated by the interfacial (i.e., due to capillary forces) pressure head. Using an

empirical fit for void fraction exiting the DMFC anode (Fig. 7) we evaluate the total pressure drop in the anode as a function of current density (Fig. 11a). As shown in Fig. 11a, the model captures the observed pressure drop trends but still requires refinement. In particular, the model captures the initial rise in pressure at low current densities and the differences in rise time associated with inlet flow rate (pressure rises slower at higher flow rates). Further, the model captures the experimentally observed trend of higher pressure drop at lower flow rates and low DMFC current densities (<0.1 A/cm^2). However, the model does not properly capture the slight differences in max pressure associated with increasing inlet flow rate (see Fig. 5a). We attribute this discrepancy to inertial and viscous effects, which currently are not accounted for in this scaling.

The empirical model does fairly well at higher current densities (>0.1 A/cm^2), which is the important region of maximum power density. This agreement is well illustrated in Fig. 11b which shows the normalized difference between predicted and measured pressure drop as a function of void fraction. At low void fraction (and current density) the empirical model for pressure drop deviates from measured pressure by a factor of two or greater. At void fractions greater than 0.5, the model adequately captures observed trends. Overall, the empirical model captures the qualitative trends observed experimentally but still requires refinement to improve its accuracy. Clearly, the prediction and optimization of DMFC anode presents both significant experimental and modeling challenges.

5. Conclusions

We performed an experimental characterization of the hydrodynamics of a DMFC anode. This study for the first time focuses on two-phase pressure drop behavior in DMFC microchannels. The flow in our DMFC anode is characterized by low capillary number (<1 × 10^{-4}) and smallest channel dimension (here, 500 μm) on the order of the predicted, characteristic CO_2 bubble detachment diameter. We designed and implemented an experimental technique to quantify two-phase flow characteristics. The technique involves a set of two ex situ optical fluidic line sensors which detect the presence of liquid or gas exiting the DMFC. These measurements provide repeatable and consistent (with void fraction predictions) measurements of void fraction, slug velocity, and liquid slug length exiting the DMFC anode.

The results of our study suggest strongly that pressure drop in our DMFC anode flow regime is dominated by interfacial (i.e., capillary) forces. Pressure drop in the DMFC anode is a complex function of methanol flow rate, CO_2 generation, and two-phase flow regime. However, we have shown that pressure drop scales with a small number of key parameters. Notably, the most effective scaling of the data is obtained by scaling pressure drop with the number of slugs, surface tension, and the diameter of the largest sphere inscribed in the channel. This pressure scaling is consistent with previous low capillary number two-phase flow studies (studies not considering DMFCs). However, unlike the previous work, our results suggest that inertial effects may significantly influence at higher void fractions (i.e., higher current densities). Inertial effects roughly scale with $Re(a/L)$, which increases monotonically with void fraction. Finally, we presented empirical correlations for the number of gas slugs and interfacial pressure which well approximate trends observed in experiments. The work provides a basis for future studies aimed at quantifying the hydrodynamic load posed by DMFC anode and at optimizing coupled fuel pump and DMFC system performance.

Future work should include characterization of two-phase flow regime and number of liquid/gas interfaces in the anode, as capillary forces can dominate anode pressure drop. Future theoretical developments should strive to combine flow models which include viscous and inertial effects in addition to capillary pressure effects.

References

[1] Y.J. Kim, B. Bae, M.A. Scibioh, E. Cho, H.Y. Ha, Behavioral pattern of a monopolar passive direct methanol fuel cell stack, J. Power Sources 157 (1) (2006) 253–259.

[2] Z. Guo, Y. Cao, A passive fuel delivery system for portable direct methanol fuel cells, J. Power Sources 132 (1–2) (2004) 86–91.

[3] D.A. Drew, Mathematical modeling of two-phase flow, Annu. Rev. Fluid Mech. 15 (1) (1983) 261–291.

[4] C. Kleinstreuer, Two-Phase Flow: Theory and Applications, Taylor & Francis, New York, 2003.

[5] D. Chisholm, A theoretical basis for the Lockhart–Martinelli correlation for two-phase flow, In. J. Heat Mass Transfer 10 (12) (1967) 1767–1778.

[6] S. Litster, N. Djilali, Two-phase transport in porous gas diffusion electrodes, in: M. Faghri, B. Sunden (Eds.), Transport Phenomena in Fuel Cells, WIT Press, Southhampton, UK, 2005.

[7] U. Pasaogullari, C.Y. Wang, Two-phase modeling and flooding prediction of polymer electrolyte fuel cells, J. Electrochem. Soc. 152 (2) (2005) A380–A390.

[8] U. Pasaogullari, C.Y. Wang, Two-phase transport and the role of micro-porous layer in polymer electrolyte fuel cells, Electrochim. Acta 49 (25) (2004) 4359–4369.

[9] A.Z. Weber, R.M. Darling, J. Newman, Modeling two-phase behavior in PEFCs, J. Electrochem. Soc. 151 (10) (2004) A1715–A1727.

[10] X. Liu, H. Guo, C. Ma, Water flooding and two-phase flow in cathode channels of proton exchange membrane fuel cells, J. Power Sources 156 (2) (2006) 267–280.

[11] T.A. Trabold, J.P. Owejan, D.L. Jacobson, M. Arif, P.R. Huffman, In situ investigation of water transport in an operating PEM fuel cell using neutron radiography. Part 1. Experimental method and serpentine flow field results, In. J. Heat Mass Transfer 49 (25–26) (2006) 4712–4720.

[12] J.B. Zhang, D. Kramer, R. Shimoi, Y. Ona, E. Lehmann, A. Wokaun, K. Shinohara, G.G. Scherer, In situ diagnostic of two-phase flow phenomena in polymer electrolyte fuel cells by neutron imaging. Part B. Material variations, Electrochim. Acta 51 (13) (2006) 2715–2727.

[13] X. Liu, H. Guo, F. Ye, C.F. Ma, Water flooding and pressure drop characteristics in flow channels of proton exchange membrane fuel cells, Electrochim. Acta 52 (11) (2007) 3607–3614.

[14] T.Z. Yan, T.-C. Jen, Two-phase flow modeling of liquid-feed direct methanol fuel cell, In. J. Heat Mass Transfer 51 (5–6) (2008) 1192–1204.

[15] Z.H. Wang, C.Y. Wang, Mathematical modeling of liquid-feed direct methanol fuel cells, J. Electrochem. Soc. 150 (4) (2003) A508–A519.

[16] A.A. Kulikovsky, Two-dimensional numerical modelling of a direct methanol fuel cell, J. Appl. Electrochem. 30 (9) (2000) 1005–1014.

[17] C. Xu, T.S. Zhao, Q. Ye, Effect of anode backing layer on the cell performance of a direct methanol fuel cell, Electrochim. Acta 51 (25) (2006) 5524–5531.

[18] P. Argyropoulos, K. Scott, W.M. Taama, Pressure drop modelling for liquid feed direct methanol fuel cells. Part 1. Model development, Chem. Eng. J. 73 (3) (1999) 217–227.

[19] H. Yang, T.S. Zhao, Q. Ye, Pressure drop behavior in the anode flow field of liquid feed direct methanol fuel cells, J. Power Sources 142 (1–2) (2005) 117–124.

[20] K. Mishima, T. Hibiki, Some characteristics of air–water two-phase flow in small diameter vertical tubes, Int. J. Multiphase Flow 22 (4) (1996) 703–712.

[21] G.Q. Lu, C.Y. Wang, Electrochemical and flow characterization of a direct methanol fuel cell, J. Power Sources 134 (1) (2004) 33–40.

[22] G.B. Wallis, One Dimensional Two Phase Flow, McGraw-Hill, New York, 1969.

[23] P. Argyropoulos, K. Scott, W.M. Taama, Carbon dioxide evolution patterns in direct methanol fuel cells, Electrochim. Acta 44 (20) (1999) 3575–3584.

[24] H. Yang, T.S. Zhao, Q. Ye, In situ visualization study of CO_2 gas bubble behavior in DMFC anode flow fields, J. Power Sources 139 (1–2) (2005) 79–90.

[25] H. Wong, C.J. Radke, S. Morris, The motion of long bubbles in polygonal capillaries. Part 1. Thin films, J. Fluid Mech. 292 (1995) 71–94.

[26] H. Wong, C.J. Radke, S. Morris, The motion of long bubbles in polygonal capillaries. Part 2. Drag, fluid pressure and fluid flow, J. Fluid Mech. 292 (1995) 95–110.

[27] F.P. Bretherton, The motion of long bubbles in tubes, J. Fluid Mech. Digital Arch. 10 (1961) 166–188.

[28] C.R. Buie, D. Kim, S. Litster, J.G. Santiago, An electro-osmotic fuel pump for direct methanol fuel cells, Electrochem. Solid State Lett. 10 (11) (2007) B196–B200.

[29] M.D. Lundin, M.J. McCready, Reduction of carbon dioxide gas formation at the anode of a direct methanol fuel cell using chemically enhanced solubility, J. Power Sources 172 (2) (2007) 553–559.

[30] T.J. Yen, N. Fang, X. Zhang, G.Q. Lu, C.Y. Wang, A micro methanol fuel cell operating at near room temperature, Appl. Phys. Lett. 83 (19) (2003) 4056–4058.

[31] H. Yang, T.S. Zhao, Effect of anode flow field design on the performance of liquid feed direct methanol fuel cells, Electrochim. Acta 50 (16–17) (2005) 3243–3252.

[32] S. Eccarius, B.L. Garcia, C. Hebling, J.W. Weidner, Experimental validation of a methanol crossover model in DMFC applications, J. Power Sources 179 (2) (2008) 723–733.

[33] F. Liu, C.-Y. Wang, Water and methanol crossover in direct methanol fuel cells: effect of anode diffusion media, Electrochim. Acta 53 (17) (2008) 5517–5522.

[34] R.Z. Jiang, C. Rong, D. Chu, Fuel crossover and energy conversion in lifetime operation of direct methanol fuel cells, J. Electrochem. Soc. 154 (1) (2007) B13–B19.

[35] J. Han, H. Liu, Real time measurements of methanol crossover in a DMFC, J. Power Sources 164 (1) (2007) 166–173.

[36] M.J. Fuerstman, A. Lai, M.E. Thurlow, S.S. Shevkoplyas, H.A. Stone, G.M. Whitesides, The pressure drop along rectangular microchannels containing bubbles, Lab Chip (7) (2007) 1479–1489.

[37] C.R. Buie, J.G. Santiago, Model and experimental study of hydrodynamic coupling between a fuel pump and a direct methanol fuel cell, ECS Trans. (2008).